FRONTIERS OF PHYSICS

RESEARCH ARTICLE
Volume 17 / Issue 5 / 53508 / 2022

Brain-like synaptic memristor based on lithium-doped silicate for neuromorphic computing

Shanwu Ke[1,*], Li Jiang[1,*], Yifan Zhao[1], Yongyue Xiao[1], Bei Jiang[1,†], Gong Cheng[1], Facai Wu[3], Guangsen Cao[1], Zehui Peng[1], Min Zhu[2,‡], Cong Ye[1]

1 Faculty of Physics and Electronic Science, Hubei University, Wuhan 430062, China
2 Shanghai Institute of Micro-system and Information Technology, Chinese Academy of Sciences, Shanghai 200050, China
3 Institute of Electronics, Chiao Tung University, Hsinchu 30010, Taiwan, China
Corresponding authors. E-mail: †jiangbei@whu.edu.cn, ‡minzhu@mail.sim.ac.cn
*These two authors contributed equally to this work.
Received March 29, 2022; accepted May 12, 2022

ABSTRACT

Artificial synapse is one of the potential electronics for constructing neural network hardware. In this work, Pt/LiSiO$_x$/TiN analog artificial synapse memristor is designed and investigated. With the increase of compliance current (C. C.) under 0.6 mA, 1 mA, and 3 mA, the current in the high resistance state (HRS) presents an increasing variation, which indicates lithium ions participates in the operation process for Pt/LiSiO$_x$/TiN memristor. Moreover, depending on the movement of lithium ions in the functional layer, the memristor illustrates excellent conduction modulation property, so the long-term potentiation (LTP) or depression (LTD) and paired-pulse facilitation (PPF) synaptic functions are successfully achieved. The neural network simulation for pattern recognition is proposed with the recognition accuracy of 91.4%. These findings suggest the potential application of the LiSiO$_x$ memristor in the neuromorphic computing.

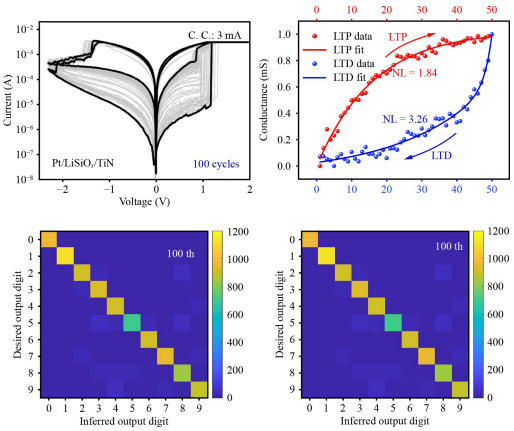

Keywords artificial synapse, lithium silicate, memristor, neuromorphic computing, resistive switching

1 Introduction

With the advent of the era of artificial intelligence, the amount of data processed by computers increases exponentially [1, 2]. However, using conventional Von Neumann architecture, today's computers are not fast and efficient enough when dealing with abundant information [3, 4]. Inspired by the biological synapses of the brain [5, 6], artificial synapses based on Resistive random access memory (RRAM) are expected to be a promising competitor for the next generation of neural network computing hardware [7]. When RRAM is used as a synaptic device, its conductance represents the weight in the neural network, so individual devices can be connected to different layers of the neural network [2]. At present, RRAM-built cross array has been applied to face recognition and other complex tasks [8, 9], and is expected to have great potential in neuromorphic computing [10, 11].

In biology, the transmission of information between synapses depends on the release of neurotransmitters into the synaptic cleft by synaptic vesicles [12, 13]. In order to simulate the information transmission mechanism of synapses, it is necessary to construct an ion transport device which is similar to the release process of synaptic transmitter [14, 15]. The conductance of cationic

https://doi.org/10.1007/s11467-022-1173-2

memristors can be continuously modulated by the accumulation or reflux of cations (such as Cu^{2+}, Ag^{+}, and Li^{+}) in the functional layer [16], which can vividly simulate the dynamic mechanism of biological synapses. As a homologous alkali metal of sodium (Na) and potassium (K) in the brain, lithium (Li) can be designed in the functional layer of memristor by doping method to mimic the synapse behavior [17, 18].

In this study, the active metal Li element is doped with silicate to fabricate the Pt/$LiSiO_x$/TiN memristor. The resistive switching (RS) behavior and conduction mechanism of the memristor are systematically investigated. Several typical synaptic plasticity properties are simulated to demonstrate the biomimetic potential of the device. Besides, the simulation of digital handwriting recognition of the is carried out to verify the capability of the device in neural network computation.

2 Experimental section

The fabrication process of the device is as follows: first, T-shaped cells with 200 nm pillar TiN bottom electrodes were fabricated using 45 nm CMOS technology. The structure diagram of these cells is shown in the inset of Fig. 1(b). Second, $LiSiO_x$ functional layer with the thickness of 10 nm was sputtered on the TiN bottom electrode by radio frequency (RF) magnetron sputtering, using a $LiSiO_x$ target (SiO_2:Li = 90:10 wt %, purity: 99.99 %) at 30 sccm (standard-state cubic centimeter per minute) under Ar gas at a working pressure of 0.3 Pa with a power of 80 W. Third, a 200 nm thick Pt electrode was sputtered on the $LiSiO_x$ film by direct current (DC) sputtering, using a Pt target (Purity: 99.99 %) under 30 sccm Ar flow with the working pressure of 0.5 Pa and the sputtering power of 100 W. Finally, the intermediate layer and the top electrode were peeled off by an ultrasonic water bath for 10 seconds.

3 Experimental results and discussion

As shown in Fig. 1(a), from the X-ray photoelectron spectroscopy (XPS) spectrum of $LiSiO_x$, the Li 1s, Si $2p_{3/2}$ and O1s signals are located at 54.9 eV, 102.1 eV, and 531.8 eV, which shows the atomic ratios of Li, Si, and O are 20.01 %, 26.45 %, and 53.54 %, respectively. Figure 1(b) and the inset show the forming process with different forming compliance current (C. C.) values of 0.6 mA, 1 mA, and 3 mA, and the structure of the Pt/$LiSiO_x$/TiN memristor. It can be observed that the forming voltage keeps at 6−7 V with different C. C.. Figures 2(a)−(c), present the $I-V$ curves of the device with different forming C. C.. It can be seen that the current distribution of the high resistance state (HRS) is stable at the C. C. of 0.6 mA, whereas the HRS value shows a broaden distribution at the C. C. of 3 mA. Moreover, it can be observed from Fig. 2(d) that the current distribution of HRS exhibits a wider trend with the increase of C. C. values. Figures S2(a)−(d) show the device to device of Pt/$LiSiO_x$/TiN memristor. It has been reported that Li ions participate in the process of conductive filament rupture/connection in $LiSiO_x$ based memristor [19, 20]. Thus, it can be speculated that the HRS of the memristor fluctuates with increasing the C. C., which may be related to the movement of Li ions in the $LiSiO_x$ layer.

To investigate the conduction mechanisms of Pt/$LiSiO_x$/TiN memristor, the typical four states $I-V$ curves of HRS at 3 mA C. C. were chosen. As shown in Figs. 3(a)−(d), all the HRS (States 1, 2, 3, 4) during the RESET process and SET process coincide with the

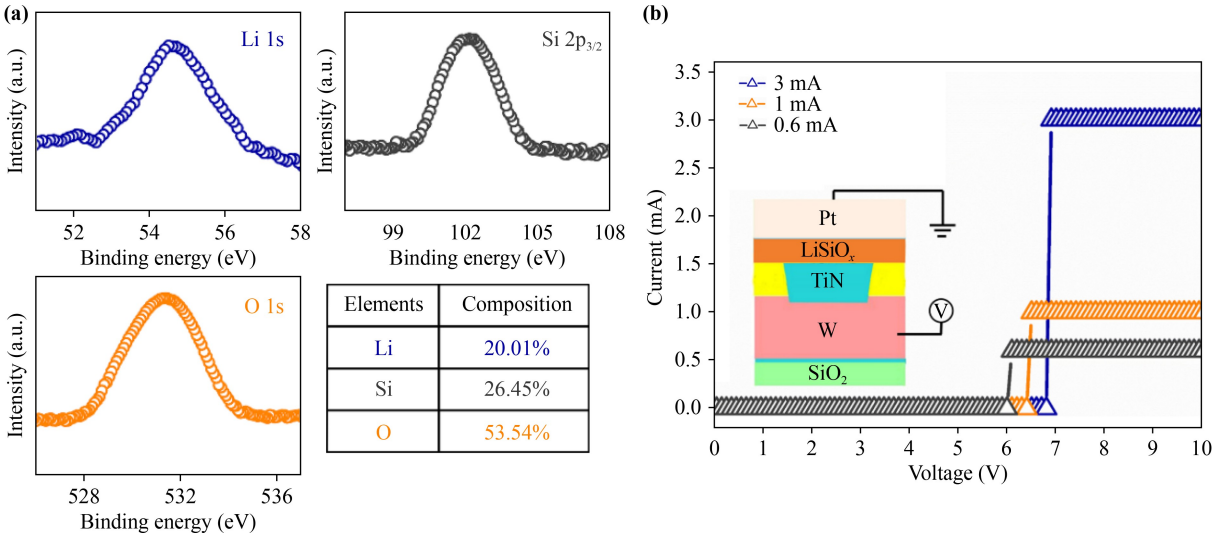

Fig. 1 **(a)** XPS spectra of the $LiSiO_x$ intermediate layer. **(b)** $I-V$ curve of the electroforming process. The inset shows the structure diagram of a T-shaped device with a 200 nm TiN pillar.

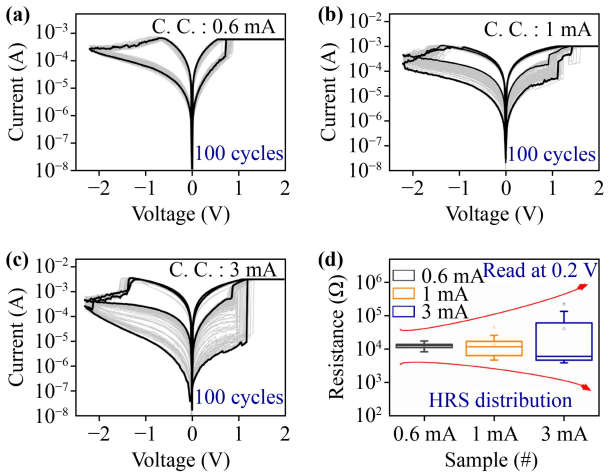

Fig. 2 **(a—c)** The I–V curves for the device under 0.6 mA, 1 mA, 3 mA C. C., respectively. **(d)** Resistance distribution for HRS, where HRS exhibits a wide resistance distribution.

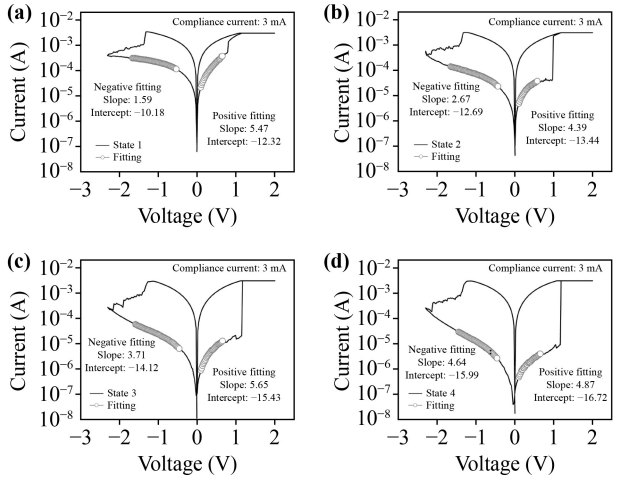

Fig. 3 **(a—d)** Four states I–V curves of HRS at 3 mA C. C. and the values for the slope and intercept of the Schottky emission fitting curves of negative and positive voltages.

Schottky emission mechanism. Figure S1 shows a linear relationship between $\ln(I)$ and $V^{1/2}$, and the slope and intercept values of the four states were listed in the inset of Fig. 3. According to the Schottky emission mechanism and the equation takes the following form [21]:

$$J = A^{**}T^2 \exp\left[\frac{-q(\Phi_{\mathrm{B}} - \sqrt{qV/(4\pi\epsilon_i d)})}{KT}\right], \tag{1}$$

where J is current density, A^{**} is the effective Richardson constant, Φ_B is barrier height, V is external voltage and ϵ_{i} is the dielectric permittivity, d is the thickness of the dielectric thin film, K is Boltzmann constant and T is temperature. By taking the logarithm of Eq. (1) and plotting the curve of $\log(I/T^2)-V^{1/2}$, the relationship between the slope and the intercept can be expressed as [21, 22]

$$\text{slope} \propto \sqrt{\frac{1}{\epsilon_i d}}, \tag{2}$$

$$|\text{Intercept}| \propto \Phi_B. \tag{3}$$

During the RESET process, it can be calculated that for the four states, with the increase of HRS value, the slope and intercept both present an increasing trend at 3 mA C. C.. It follows from Eq. (2) and Eq. (3) that the slopes are inversely proportional to the square root of the product of the film thickness and the dielectric constant. Meanwhile, the intercept is proportional to the barrier height and increases for four states, thus the Schottky distance increases. From prior literature, TiN electrode can attract and store lithium ions under the action of electrical stress [23–25]. Therefore, it can be deduced that a lithium-rich layer was formed on the side of TiN electrode during the RESET process [26]. This will result in the concentration drop of Li in the functional layer, making the dielectric near the TiN electrode much more like silicon oxide [19]. Thus, the dielectric constant will decrease, reflecting as the slope rise in the conduction current fitting curves in Fig. 3(b). And the increase of silicon oxide concentration in the functional layer may lead to the rise of barrier height, which externally manifested by the gradual increase of the intercept absolute value [27–29]. Furthermore, the thickness of the lithium-rich layer formed near the TiN electrode is random due to the high activity of lithium ions, which leads to random shrinkage of the conductive filaments (CFs). And the 4 states of memristor mechanism for positive voltage also coincide with the Schottky emission mechanism. After fitting positive voltage of $I-V$ curves, it is found that the intercept will increase with the increase of memory window, such as 4 states of negative voltage. However, the slopes of positive voltage for State 1 to State 4 are 5.47, 4.39, 5.65, 4.87. Different from the negative fitting data, the slope of the positive for high resistance state remain a stable number. The reason for this phenomenon is that lithium ions rapidly drift towards Pt electrode under the action of electric field force in the Set process, and the dielectric constant of the dielectric layer near TiN electrode does not change significantly.

Figure 4 illustrates the conductive filaments conduction mechanism of Pt/LiSiO$_x$/TiN device to explain and depict the experimental results above. In the SET process, Li—Si—O bond fracture causes the Li ions in the intermediate layer to drift to the Pt electrode [Fig. 4(a)] [30–33]. As shown in Figs. 4(b)—(e), during the RESET process, Li ions transfer to the TiN electrode under the negative bias [23]. It leads to the accumulation of Li ions near the TiN electrode, forming a lithium-rich layer, as illustrated in Fig. 4. According to Fig. 3(b), from State 1 to State 4, the Schottky distance increases, which indicates the CF rupture distance increases, as shown in Figs. 4(b)—(e). Therefore, it leads to the highest resistance

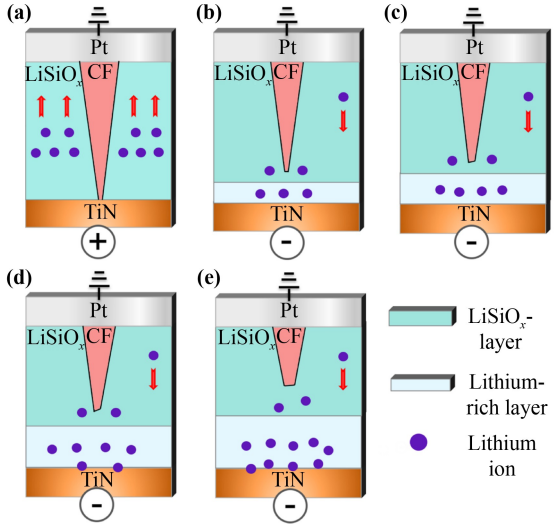

Fig. 4 **(a)** Schematic diagram of RS mechanism of the LRS for the device. **(b—e)** Four states of HRS process for Pt/LiSiO$_x$/TiN device under the 3 mA C. C..

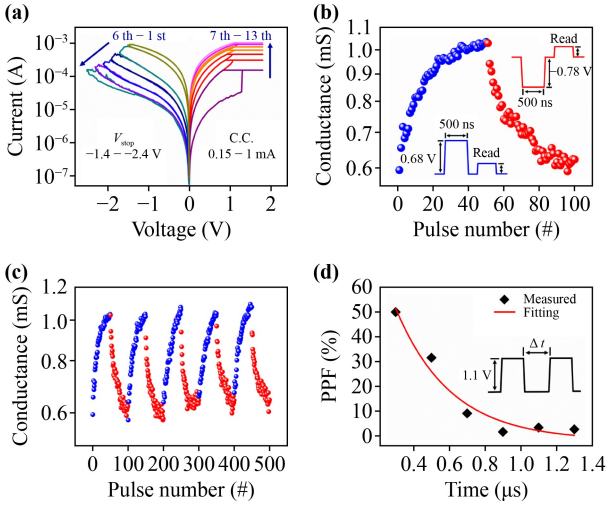

Fig. 5 **(a)** $I-V$ curves of the Pt/LiSiO$_x$/TiN memristor by a continuous negative bias sweep with the stop voltage amplitudes increasing from −1.4 to −2.4 V followed by a continuous positive voltage sweeps with C. C. value increasing from 0.15 mA to 1 mA. **(b)** Conductance (or synaptic weight) modulation under repeated positive (potentiation) or negative (depression) spikes. **(c)** Five cycles of the (b) at 0.2 V read voltages. **(d)** Two pairs of pulses (1.1 V, 1 μs) were applied at six different spike time intervals, the PPF effect was obtained. By fitting the measured PPF value, the spike-time dependence curve was obtained.

value of the State 4, which is also attributed to the most Li ions accumulating near the TiN electrode and forming the thickest lithium-rich layer.

Biological synapses are located between the axons and dendrites of two neurons [34, 35]. The conductance modulation effect of memristors is similar to the weight regulation of biological synapses, which allows the memristors to simulate many biological transport characteristics. Figure 5(a) illustrates the $I-V$ curve of the Pt/LiSiO$_x$/TiN memristor through continuous negative bias sweep with stop voltage amplitude increase from −1.4 V to −2.4 V, and then continuous positive setting voltage sweep, the C. C. value increased from 0.15 mA up to 1 mA, the process of gradual "RESET" and "SET" can be clearly seen [36]. The stable conductance modulation under DC provides reliability for simulating the voltage spikes behavior of artificial biological synapses. Figure 5(b) shows 50 potentiation spikes and 50 depression spikes were applied on the device. The duration of potentiation spikes and depression spikes was 500 ns, and the amplitude was 0.68 V and −0.78 V, respectively. At the end of each spike, a 0.2 V read voltage was applied to read the device conductance. The process named long-term potentiation (LTP), long-term depression (LTD) of synapses. Figure S3 shows that the nonlinear factors of LTP and LTD are 1.84 and 3.26, respectively [37]. Figure 5(c) was Fig. 5(b) for five consecutive periods. For a pair of pulses, the second pulse current can be several times larger than the first pulse current. This effect was analogous to the paired-pulse facilitation (PPF) [38]. Figure 5(d) shows PPF effect at six different intervals with a pair of pulses. The time interval between the first pulse and the second pulse is 0.3 μs, 0.5 μs, 0.7 μs, 0.9 μs, 1.1 μs, and 1.3 μs. With the increase of pulse time interval, the enhancement of the second pulse current will gradually attenuate. The PPF ratio can be defined as follows:

$$\text{PPF ratio} = \frac{p_2 - p_1}{p_1} \times 100\%, \tag{4}$$

in which p_1 and p_2 are the response current values of the first pulse and the second pulse. Then, Fig. 5(d) fits the PPF ratio with the measured data. And the fitting results show that the PPF ratio presents a downward trend.

In order to demonstrate the potential of the device in the field of neuromorphic computing, a 784×64×10 three-layer (input layer, hidden layer, and output layer) convolutional neural network was simulated to test the accuracy of Mixed National Institute of Standards and Technology (MNIST) handwritten dataset [39–41]. The MNIST handwritten dataset contains 60 000 training pictures and 10 000 test pictures, all of which are initialized to 28×28 pixels. The 784 pixels values of each image are encoded as input, and the result was obtained by convolute calculation in the hidden layer and the output layer. Each time there was an error between the calculated result and the correct result, the weight in the connection layer was corrected according to the error, until the error was within an acceptable range. The process of calculation is called "training", and the number of training depends on whether the error continues to decrease. Figures 6(a)—(c) present the chaotic matrix for 10 digits

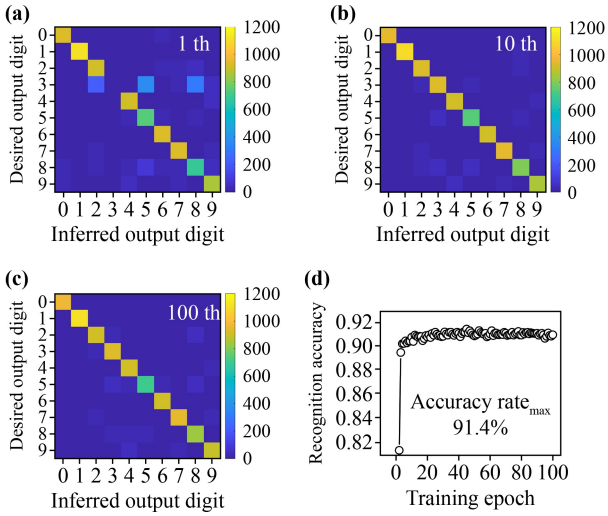

Fig. 6 **(a—c)** Chaotic matrix is based on the simulation test results of MNIST test set. They were trained for 1 time, 10 times, and 100 times respectively. **(d)** The recognition accuracy increases with the training times.

from the MNIST test set of 1 time, 10 times and 100 times training. The LTP and LTD data in Fig. 5(b) were used as the adjustment parameter of the weights in the neural network. After 23 epochs of training, the simulation network recognition accuracy can reach 91%, and it converged to 91.4% after 100 times of training (as shown in Fig. 6(d)). The results show that the device has a promising application in the field of neural network computing.

4 Conclusion

In this work, a Pt/LiSiO$_x$/TiN memristor based on lithium-doped silicate has been established. Due to the movement of Li ions during operation, the memristor exhibits excellent conductivity modulation properties. The synaptic biomimetic properties of LTD, LTP, PPF have been simulated successfully by this synaptic device. The accuracy of MNIST pattern recognition using an analog cross array memristors for MNIST pattern recognition reached 91.4%. The results show that this memristor has great potential for neuromorphic computing in the future.

Electronic supplementary materials are available in the online version of this article at https://doi.org/10.1007/s11467-022-1173-2 and https://journal.hep.com.cn/fop/EN/10.1007/s11467-022-1173-2 and are accessible for authorized users.

Acknowledgements This work was supported by the Strategic Priority Research Program of the Chinese Academy of Sciences under Grant No. XDB44000000 and the National Natural Science Foundation of China (No. 61774057).

References

1. M. Prezioso, F. Merrikh-Bayat, B. D. Hoskins, G. C. Adam, K. K. Likharev, and D. B. Strukov, Training and operation of an integrated neuromorphic network based on metal-oxide memristors, *Nature* 521(7550), 61 (2015)
2. H. Wu, M. Zhao, Y. Liu, P. Yao, Y. Xi, X. Li, W. Wu, Q. Zhang, J. Tang, B. Gao, and H. Qian, Reliability perspective on neuromorphic computing based on analog RRAM, *IEEE Int. Reliab. Phys. Symp.* 1—4 (2019)
3. R. Schmitt, M. Kubicek, E. Sediva, M. Trassin, M. C. Weber, A. Rossi, H. Hutter, J. Kreisel, M. Fiebig, and J. L. Rupp, Accelerated ionic motion in amorphous memristor oxides for nonvolatile memories and neuromorphic computing, *Adv. Funct. Mater.* 29(5), 1804782 (2019)
4. P. A. Merolla, J. V. Arthur, R. Alvarez-Icaza, A. S. Cassidy, J. Sawada, F. Akopyan, B. L. Jackson, N. Imam, C. Guo, Y. Nakamura, B. Brezzo, I. K. Esser, R. Appuswamy, B. Taba, A. Amir, M. D. Flickner, W. P. Risk, R. Manohar, and D. S. Modha, A million spiking-neuron integrated circuit with a scalable communication network and interface, *Science* 345(6197), 668 (2014)
5. C. Zhang, J. Shang, W. Xue, H. Tan, L. Pan, X. Yang, S. Guo, J. Hao, G. Liu, and R. W. Li, Convertible resistive switching characteristics between memory switching and threshold switching in a single ferritin-based memristor, *Chem. Commun.* 52(26), 4828 (2016)
6. Z. Wang, S. Joshi, S. E. Savel'ev, H. Jiang, R. Midya, P. Lin, M. Hu, N. Ge, J. P. Strachan, Z. Li, Q. Wu, M. Barnell, G. L. Li, H. L. Xin, R. Williams, Q. F. Xia, and J. J. Yang, Memristors with diffusive dynamics as synaptic emulators for neuromorphic computing, *Nat. Mater.* 16(1), 101 (2017)
7. L. Du, Z. Wang, and G. Zhao, Novel intelligent devices: Two-dimensional materials based memristors, *Front. Phys.* 17(2), 23602 (2022)
8. P. Yao, H. Wu, B. Gao, S. B. Eryilmaz, X. Huang, W. Zhang, Q. Zhang, N. Deng, L. Shi, H. S. P. Wong, and H. Qian, Face classification using electronic synapses, *Nat. Commun.* 8(1), 15199 (2017)
9. P. N. Belhumeur, J. P. Hespanha, and D. J. Kriegman, Eigenfaces vs. Fisherfaces: Recognition using class specific linear projection, *IEEE. T. Pattern Anal.* 19(7), 711 (1997)
10. H. L. Park, M. H. Kim, and S. H. Lee, Reliable organic memristors for neuromorphic computing by predefining a localized ion-migration path in crosslinkable polymer, *Nanoscale* 12(44), 22502 (2020)
11. Y. Li, Z. Wang, R. Midya, Q. Xia, and J. J. Yang, Review of memristor devices in neuromorphic computing: Materials sciences and device challenges, *J. Phys. D Appl. Phys.* 51(50), 503002 (2018)
12. G. Liu, C. Wang, W. Zhang, L. Pan, C. Zhang, X. Yang, F. Fan, Y. Chen, and R. W. Li, Organic biomimicking memristor for information storage and processing applications, *Adv. Electron. Mater.* 2(2), 1500298 (2016)
13. J. Yin, F. Zeng, Q. Wan, F. Li, Y. Sun, Y. Hu, J. L.

Liu, G. Q. Li, and F. Pan, Adaptive crystallite kinetics in homogenous bilayer oxide memristor for emulating diverse synaptic plasticity, *Adv. Funct. Mater.* 28(19), 1706927 (2018)
14. S. Kim, C. Du, P. Sheridan, W. Ma, S. Choi, and W. D. Lu, Experimental demonstration of a second-order memristor and its ability to biorealistically implement synaptic plasticity, *Nano Lett.* 15(3), 2203 (2015)
15. Y. Park and J. S. Lee, Artificial synapses with short- and long-term memory for spiking neural networks based on renewable materials, *ACS Nano* 11(9), 8962 (2017)
16. M. N. Kozicki, and H. J. Barnaby, Conductive bridging random access memory-materials, devices and applications, *Semicond. Sci. Technol.* 31(11), 113001 (2016)
17. T. V. P. Bliss and G. L. Collingridge, G. L. A synaptic model of memory: Long-term potentiation in the hippocampus, *Nature* 361(6407), 31 (1993)
18. X. M. Zhang, S. Liu, X. L. Zhao, F. C. Wu, Q. T. Wu, W. Wang, and M. Liu, Emulating short-term and long-term plasticity of bio-synapse based on Cu/a-Si/Pt memristor, *IEEE Electron Device Lett.* 38(9), 1208 (2017)
19. K. C. Chang, T. M. Tsai, and T. C. Chang, Dual ion effect of the lithium silicate resistance random access memory, *IEEE Electron Device Lett.* 35(5), 530 (2014)
20. J. Chen, C. Y. Lin, Y. Li, C. Qin, K. Lu, J. M. Wang, C. K. Chen, Y. H. He, T. C. Chang, and X. S. Miao, $LiSiO_x$-based analog memristive synapse for neuromorphic computing, *IEEE Electron Device Lett.* 40(4), 542 (2019)
21. Y. L. Hsieh, W. H. Su, C. C. Huang, and C. Y. Su, Solution-processed black phosphorus nanoflakes for integrating nonvolatile resistive random-access memory and the mechanism unveiled, *Nanotechnology* 30(44), 445702 (2019)
22. L. Liu, W. Xiong, Y. Liu, K. Chen, Z. Xu, Y. Zhou, J. Han, C. Ye, X. Chen, Z. T. Song, and M. Zhu, Designing high-performance storage in $HfO_2/BiFeO_3$ memristor for artificial synapse applications, *Adv. Electron. Mater.* 6(2), 1901012 (2020)
23. Y. C. Qiu, K. Y. Yan, S. H. Yang, L. M. Jin, H. Deng, and W. S. Li, Synthesis of size-tunable anatase TiO_2 nanospindles and their assembly into anatase@ titanium oxynitride/titanium nitride graphene nanocomposites for rechargeable lithium-ion batteries with high cycling performance, *ACS Nano* 4(11), 6515 (2010)
24. Y. H. Yue, P. X. Han, S. M. Dong, K. J. Zhang, C. J. Zhang, C. Q. Shang, and G. L. Cui, Nanostructured transition metal nitride composites as energy storage material, *Chin. Sci. Bull.* 57(32), 4111 (2012)
25. M. Q. Snyder, S. A. Trebukhova, B. Ravdel, M. C. Wheeler, J. DiCarlo, C. P. Tripp, and W. J. DeSisto, Synthesis and characterization of atomic layer deposited titanium nitride thin films on lithium titanate spinel powder as a lithium-ion battery anode, *J. Power Sources* 165(1), 379 (2007)
26. C. Y. Lin, J. Chen, P. H. Chen, T. C. Chang, Y. Wu, J. K. Eshraghian, J. Moon, S. Yoo, Y. H. Wang, W. C. Chen, Z. Y. Wang, H. C. Huang, Y. Li, X. Miao, W. D. Lu, and S. M. Sze, Adaptive synaptic memory via lithium ion modulation in RRAM devices, *Small* 16(42), 2003964 (2020)
27. H. J. Zhang, C. T. Cheng, H. Zhang, R. Chen, B. J. Huang, H. D. Chen, and W. H. Pei, Physical mechanism for the synapse behaviour of $WTiO_x$-based memristors, *Phys. Chem. Chem. Phys.* 21(42), 23758 (2019)
28. Y. Li, K. S. Yin, M. Y. Zhang, L. Cheng, K. Lu, S. B. Long, and X. S. Miao, Correlation analysis between the current fluctuation characteristics and the conductive filament morphology of HfO_2-based memristor, *Appl. Phys. Lett.* 111(21), 213505 (2017)
29. Y. Fu, B. Dong, W. C. Su, C. Y. Lin, K. J. Zhou, T. C. Chang, and X. S. Miao, Enhancing $LiAlO_x$ synaptic performance by reducing the Schottky barrier height for deep neural network applications, *Nanoscale* 12(45), 22970 (2020)
30. E. Sivonxay, M. Aykol, and K. A. Persson, The lithiation process and Li diffusion in amorphous SiO_2 and Si from first-principles, *Electrochim. Acta* 331, 135344 (2020)
31. Y. Zhang, Y. Li, Z. Wang, and K. Zhao, Lithiation of SiO_2 in Li-ion batteries: *in situ* transmission electron microscopy experiments and theoretical studies, *Nano Lett.* 14(12), 7161 (2014)
32. J. Moon, Tailoring the oxygen content in lithiated silicon oxide for lithium-ion batteries, *Int. J. Energy Res.* 45(5), 7315 (2021)
33. Z. Zhou, F. Yang, S. Wang, L. Wang, X. Wang, C. Wang, and Q. Liu, Emerging of two-dimensional materials in novel memristor, *Front. Phys.* 17(2), 1 (2022)
34. R. S. Zucker and W. G. Regehr, Short-term synaptic plasticity, *Annu. Rev. Physiol.* 64(1), 355 (2002)
35. A. J. Smith, S. Owens, and I. D. Forsythe, Characterisation of inhibitory and excitatory postsynaptic currents of the rat medial superior olive, *J. Physiol.* 529(3), 681 (2000)
36. P. Li, Z. M. Gao, X. S. Huang, L. F. Wang, W. F. Zhang, and H. Z. Guo, Ferroelectric polarization reversal tuned by magnetic field in a ferroelectric $BiFeO_3$/Nb-doped $SrTiO_3$ heterojunction, *Front. Phys.* 13(5), 1 (2018)
37. P. Y. Chen, B. Lin, I. T. Wang, T. H. Hou, J. Ye, S. Vrudhula, and S. Yu, Mitigating effects of non-ideal synaptic device characteristics for on-chip learning, in: *Proc. IEEE/ACM Int. Conf. Comput. Aided Design (ICCAD)*, 194–199 (2015)
38. P. P. Atluri and W. G. Regehr, Determinants of the time course of facilitation at the granule cell to Purkinje cell synapse, *J. Neurosci.* 16(18), 5661 (1996)
39. W. Q. Pan, J. Chen, R. Kuang, Y. Li, Y. H. He, G. R. Feng, and X. S. Miao, Strategies to improve the accuracy of memristor-based convolutional neural networks, *IEEE Trans. Electron Dev.* 67(3), 895 (2020)
40. H. Sun, Z. Luo, C. Liu, C. Ma, Z. Wang, Y. Yin, and X. Li, A flexible $BiFeO_3$-based ferroelectric tunnel junction memristor for neuromorphic computing, *Journal of Materiomics* 8(1), 144 (2022)
41. J. Lee, J. H. Ryu, B. Kim, F. Hussain, C. Mahata, E. Sim, and S. Kim, Synaptic characteristics of amorphous boron nitride-based memristors on a highly doped silicon substrate for neuromorphic engineering, *ACS Appl. Mater. Interfaces* 12(30), 33908 (2020)